Analysis of the excavation deviations impact on geological radioactive waste repository performance

Alain Genty, Christophe Le Potier, Stéphane Gounand

Geotechnical and Geological Engineering manuscript No.
(will be inserted by the editor)

Analysis of the excavation deviations impact on geological radioactive waste repository performance

Alain Genty · Christophe Le Potier · Stéphane Gounand

Received: date / Accepted: date

Abstract Numerical simulations of the transport of radionuclide from high-level radioactive waste stored in geological repositories often do not take into account construction defects in the repository. The potential impact of drilling and excavation deviation from the engineer planned design is *a priori* considered negligible. We conducted computations on repository geometries that contain deviations from horizontal of a few degrees. The analysis of the results shows that the impact of deviation defects varies from 9 to 16 percent. A perfect control of the galleries and waste repository cell orientations is then of concern for radioactive waste repository construction, failing which numerical simulations must be conducted on the worst geometric configuration or margin errors added. On the other hand, if the orientation control is precise enough, a modification of the repository design including controlled deviations from the horizontal may be of interest.

Keywords radioactive waste repository · excavation deviation · radionuclide transport calculation

1 Introduction

Many countries producing high-level radioactive waste from nuclear power plants are studying repositories in deep geological formations as a potential storage option [2,40,42]. The basic idea of the deep geological repository consists in isolating inside a geological formation the radionuclides from the biosphere for a long period of time, thereby reducing the radionuclide activity by radioactive decay. With regards to the half life of radionuclides of interest (15.7 million years for ^{129}I), this long period of time will last hundreds of thousands to millions of years. Regardless of the containment method, radionuclides will eventually leak into the surrounding geological porous media. Water filling the pores will be then the vehicle transport of radionuclides towards the biosphere. In order to delay the radionuclide transport to the biosphere, the repositories are chosen in deep formations (several hundreds of meters deep) with low water content like salt [37] or with low permeability like granite [6] or argillaceous media [2,40,42].

The general conceptual design of a radioactive waste repository architecture includes a shaft (or a set of shafts) that permits access to the underground repository level and a set of connecting galleries giving access to waste repository cells. Shapes and dimensions of the repository components depend on the kind of waste to be stored (spent fuel, vitrified waste, other reprocessing waste), on the geological host rock chosen and on specific national prevailing choices.

Numerical simulations of flow and radionuclide transport have been extensively performed for radioactive waste repository studies [10,32,5,29]. Thus, numerical simulation is appropriate to access the large time span of interest of the system (over 1 million years) as well as the large spatial scales to be considered including waste canisters of meter extension embedded in geological formations of kilometer extension. Numerical simulation is then a useful tool to address the waste repository concept performance issues including repository design, waste conditioning and back-filling materials properties.

A. Genty · C. Le Potier · S. Gounand
Commissariat à l'Énergie Atomique et aux Énergies Alternatives,
CEA-Saclay, DEN DM2S SFME,
91191 Gif sur Yvette Cedex, France
Tel.: +33-1-69088357
Fax: +33-1-69085242
E-mail: alain.genty@cea.fr

To our knowledge, previous numerical simulations have always been conducted on "perfect" repository geometries. Defects induced when excavating galleries and repository vaults are *a priori* considered negligible. One of those potential defects is the excavation deviation from the planned direction that can result in non-horizontal galleries and repository vaults. In this paper, we will focus on the impact on the repository performance of this excavation deviation defect.

Note that the impact on the repository performance of the uncertainties on transport parameter values like host-rock permeability or diffusion coefficient can be estimated using sensitivity analyses techniques [24,19, 15] and devoted numerical tools [23,21]. Note that those studies do not take into account the impact of the excavation deviations, of uncertainties on dimensions nor of the accuracy of the numerical calculations. The conclusions of those sensitivity analyses are found to be qualitative and case-specific with, for example, the definition of the advective flow rate as the most important parameter for a granitic host-rock concept [19] and the definition of the diffusive flow rate as the most important parameter for an argillaceous host-rock concept [35].

2 Description of the repository design

Existing different designs of repository architecture depend mainly on the kind of radioactive waste to dispose. We focused on the French vitrified waste repository design described in [2,8] and devoted to the isolation of radioactive waste resulting from spent fuel reprocessing.

2.1 Geological description

In France, the Callovo-Oxfordian argilites (150 Ma) are a very low permeable geological layer of interest for potential building of a radioactive waste repository. Sandwiched by calcareous Oxfordian (on the top) and carbonaceous Dogger (on the bottom) aquifers, the 100 meters thick argillaceous rock located between 450 and 550 meters deep [10] around the deep-seated research laboratory of Bure (Meuse, France) is of particular interest [17,2] due to the very low permeability ($10^{-13}\, m \cdot s^{-1}$) of this kind of rock [10,34,25,18].

2.2 Geometry of the repository

The general design of the French repository is presented in Figure 1. It includes a vertical shaft that permits access to the middle of the host rock layer and a network of horizontal connecting galleries that contain horizontal repository cells in which vitrified waste canisters will be inserted. The repository architecture is then essentially horizontal and is chosen to present dead end repository cells in order to avoid water flow inside repository and connecting galleries network. Repository components shape and dimensions, materials used as well as material properties will be described in next section. Cylindrical vitrified waste canisters (1.34 meter long, 0.43 meter in diameter [2]) are expected to be inserted in horizontal repository cells with 30 meters useful length [2,8]. In order to limit the maximum temperature of the canisters of the exothermic vitrified wastes, inert ceramic boxes will separate the canisters, and so a repository cell will contain on the order of ten canisters. As the total number of vitrified waste canisters is expected to be of the order of 36,000 [2], a total of about 3,600 repository cells is to be considered. Finally, the repository extension will cover about $9\, km^2$.

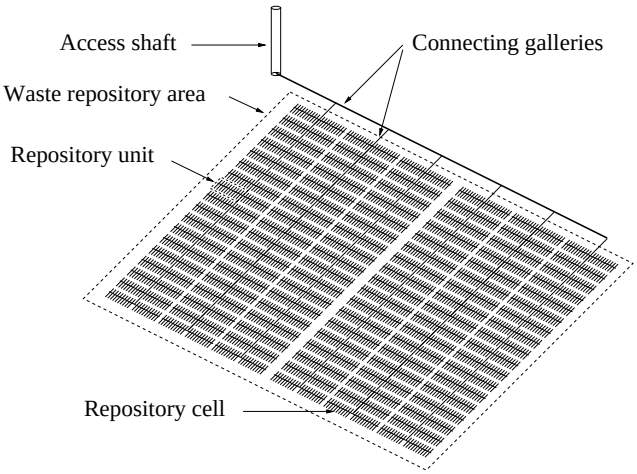

Fig. 1 General design of the French vitrified waste repository concept

2.3 Geometry of the repository unit

The flow and radionuclide transport calculation on the whole repository geometry is beyond the reach of computational resources. An efficient way to deal with performance assessment of such kind of repository then consists of performing the needed computation on elementary parts of the system like the repository unit shown in Figure 1. The chosen repository unit includes a dead end connecting gallery allowing access to a double row of 10 waste repository cells. A horizontal cut top view of the selected repository part is presented in Figure 2. The repository unit, is then embedded in an

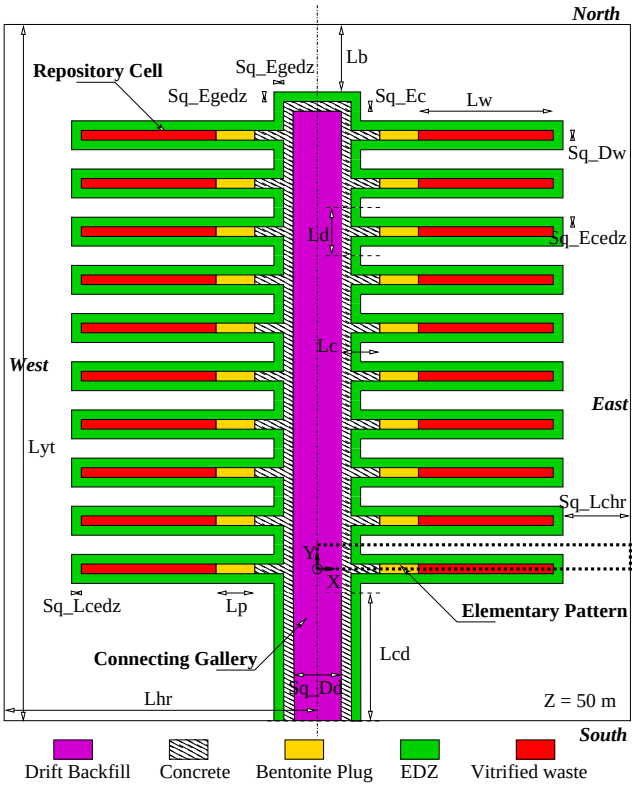

Fig. 2 Horizontal cut (middle of the host rock) top view of the selected part of the repository

argillaceous box two times Lhr long in x direction, Lyt long in y direction and Hhr long in z direction. We choose to locate the bottom boundary at $z = 0\,m$ and the top boundary at $z = Hhr = 100\,m$. The horizontal plane located at $z = 50\,m$ can be considered a symmetry plane. In order to easily locate the boundaries of the repository unit box, an arbitrary axis system is drawn in Figure 2 including North, South, East and West lateral boundary locations.

The repository unit components not only consist of repository cells filled with waste canisters and of a connecting gallery filled with backfill material just before repository closure but also of engineered materials (Cf. Figure 2). Bentonite and concrete plugs are used to seal the repository cells. Concrete is also used at the walls of the galleries to strengthen the mechanical resistance of the repository and to reduce damaging the host rock walls during the operation stage of the repository. Finally, gallery and repository cell excavation are known to damage the host rock at the repository walls [7,12,28,46]. This damaged host rock area is called the Excavation Damaged Zone (EDZ) and surrounds the repository [9,26,31]. Properties of the EDZ material are considered very different from those of the unaltered geologic rock [17]. As a result, EDZ is considered to be a different material.

We assume that the cross sections of waste repository cells and galleries are square instead of circular. This simplification allow us to build a very simple mesh of the repository unit and is known to have an impact on radionuclide activity fluxes far from the sources of about 5 percent [22]. A three dimensional representation of the elementary pattern of the repository unit identified in Figure 2 is shown in Figure 3.

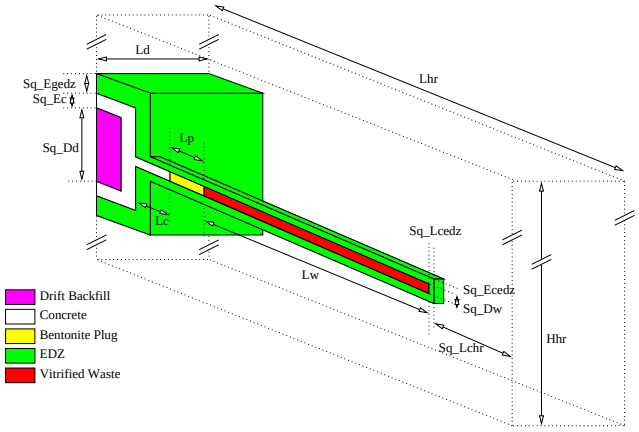

Fig. 3 Simplified 3D geometry of a half waste repository cell connected to a half gallery section. Argillaceous host rock filling the dotted box is not shown.

The repository components' dimensions depicted in Figure 2 and in Figure 3 are taken from [2,8] and the numerical values are presented in Table 1.

A three dimensional view of the repository unit is shown in Figure 4.

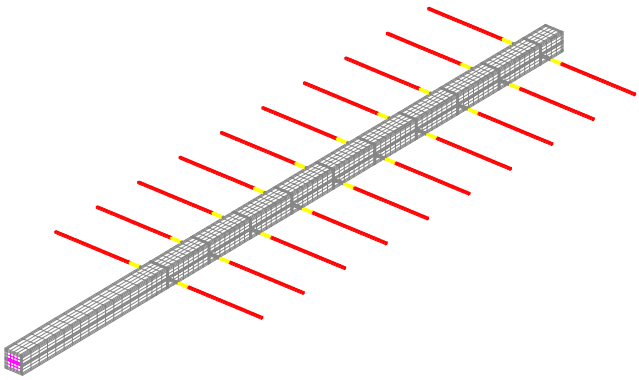

Fig. 4 Three dimensional view of the repository unit (without host rock and EDZ).

3 Excavation deviation

Previous flow and radionuclide transport computations performed on the repository design presented above

Table 1 Repository unit components dimensions

Name	Description	Value (m)
Sq_Dw	Cell repository diameter	0.62
Sq_Dd	Gallery inner diameter	5.32
Sq_Ec	Gallery concrete extension	0.885
Sq_Egedz	Gallery EDZ extension	1.77
Sq_Ecedz	Repository cell EDZ extension	0.155
Sq_Lcedz	Repository cell end EDZ extension	0.155
Sq_Lchr	Host rock extension at the end of repository cell	10.475
Lc	Concrete plug length	4
Lp	Bentonite plug length	4
Lw	Waste repository cell plug length	30
Ld	Gallery length (half distance between axes of neighbor cells)	30
Lhr	Elementary pattern length	52.175
Lcd	Connecting gallery length between the first repository cell and southern boundary	60
Lb	Host rock extension between the gallery EDZ and northern boundary	60
Lyt	Total length of the repository unit in y direction	322.655
$2 \times Lhr$	Total length of the repository unit in x direction	104.35
Hhr	Host rock vertical extension	100

have always considered the repository geometry with no geometrical defects. Engineers working in geotechnical fields such as petroleum engineering know well that boreholes always deviate from the planned direction [33] and they have therefore developed models [43] and measurement techniques [38]. In the next subsections we conducted a short review on excavation deviation measurements in order to obtain some typical values of the possible repository cells and gallery deviation from the theoretical horizontal.

3.1 Gallery excavation

Standard techniques used for gallery excavation are the drill and blast technique, the mechanical excavation and the percussion drilling techniques [4]. The drill and blast technique consists of drilling short boreholes (few meters long) at the cutting edge of the gallery, filling those boreholes with explosives and blasting the rock. The mechanical excavation technique uses rotating cutters assembled on mobile miner or tunnel boring machines. The percussion drilling technique use a pneumatic percussion drill. Whichever the technique used, deviation from the planned direction is less problematic than for the smaller waste repository cells drilling because the operator is situated inside the gallery and is able to continuously check the gallery direction and to correct the possible deviation. Nevertheless, despite efforts to correct deviations during construction, there will always be a deviation of the gallery from the planned direction and a 2° deviation must be taken into account [4].

3.2 Repository cell excavation

The repository cells' dimensions are 30 meters in length and 0.62 meters in diameter and have to be excavated from an underground gallery of 5.32 meters in diameter. One method consists of using a micro tunnel boring machine or a guided reamer (0.62 meter in diameter) guided along a borehole previously drilled [4,8]. The deviation from horizontal of the repository cells will then be the one of the drilled borehole.

Borehole deviation from the planned direction can be caused by setup error or by instability of the drill platform and rod. It also depends on the rock properties and is very sensitive for layered and anisotropic rocks [43] like the Callovo-Oxfordian argilites. Finally, the physics of the drilling (hole advance rate and rotation speed) can create forces which can amplify the rate of deviation [33]. Values of typical borehole deviation from the expected direction vary from about 2° [47,14, 4] to about 10° [20,44] and drillers considers a classical value of 5° [20,45,39].

3.3 Tested repository unit geometry

In order to test the effects of galleries and repository cell deviations from the expected direction on flow and transport calculations results, we chose to use four altered repository unit geometries. The four altered geometries were constructed from the no-defect geometry presented in Figure 4 on which flow and transport calculation result will be considered as a reference. We first assume that the central part of the repository unit, namely the gallery part where repository cells are connected (Cf. Figure 4), is perfectly horizontal. We chose

to only consider deviation from the horizontal. We use θ_c to denote the deviation angle of the repository cell from the horizontal and we consider two possible values of $\theta_c = +5°$ for upward deviation and $\theta_c = -5°$ for downward deviation. We use θ_g to denote the deviation angle of the entrance part of the gallery (the part of the gallery not linked with repository cells in Fig. 4) from the horizontal (and then from the central part of the repository unit direction) and we consider two possible values of $\theta_g = +2°$ for upward deviation and $\theta_g = -2°$ for downward deviation. The combination of the θ_c and θ_g selected angles then leads to the four geometries presented in Figure 5.

4 Numerical model

The steady state water flow equation we consider here [30] is given by relation (1)

$$\begin{cases} div\,\mathbf{U} = 0 \\ \mathbf{U} = -\bar{K}\,\nabla H \end{cases} \tag{1}$$

where $\mathbf{U}$ $[m \cdot s^{-1}]$ is the Darcy velocity, H $[m]$ is the head and $\bar{K}$ $[m \cdot s^{-1}]$ is the permeability tensor.

The radionuclide transport equation [30] is given by

$$\omega \frac{\partial C}{\partial t} = \nabla \cdot (\bar{D} \nabla C - C\mathbf{U}) - \omega \lambda C + Q \tag{2}$$

where ω $[-]$ is the porosity, λ $[s^{-1}]$ is the radioactive decay constant, C $[mol \cdot m^{-3}]$ is the solute concentration, Q $[mol \cdot m^{-3} \cdot s^{-1}]$ is a source term and $\bar{D} = \bar{D}_e + \bar{\alpha}\mathbf{U}$ $[m^2 \cdot s^{-1}]$ is the dispersive tensor (expressed in velocity coordinates) where $\bar{D}_e$ $[m^2 \cdot s^{-1}]$ is the effective diffusion tensor and $\bar{\alpha}$ $[m]$ is the dispersivity tensor. Note that in velocity coordinates, the dispersivity tensor $\bar{\alpha}$ is fully determined by α_L $[m]$ and α_T $[m]$ the longitudinal and transverse dispersivities respectively.

The resolution of equations (1) and (2) were performed using the numerical tool CASTEM [13].

4.1 Numerical scheme

We solve equation (1) numerically using the Mixed Hybrid Finite Elements (MHFE) method [11,16].

Equation (2) was solved using an implicit time discretization scheme and a finite volume method using the Multi-Point Flux Approximation (MPFA) [1,27] for the spatial scheme.

The resulting associated linear systems were solved using the bi-conjugate gradient stabilized method (Bi-CGSTAB) [41] and an incomplete LU factorization with dual truncation strategy preconditioner (ILUT) [3].

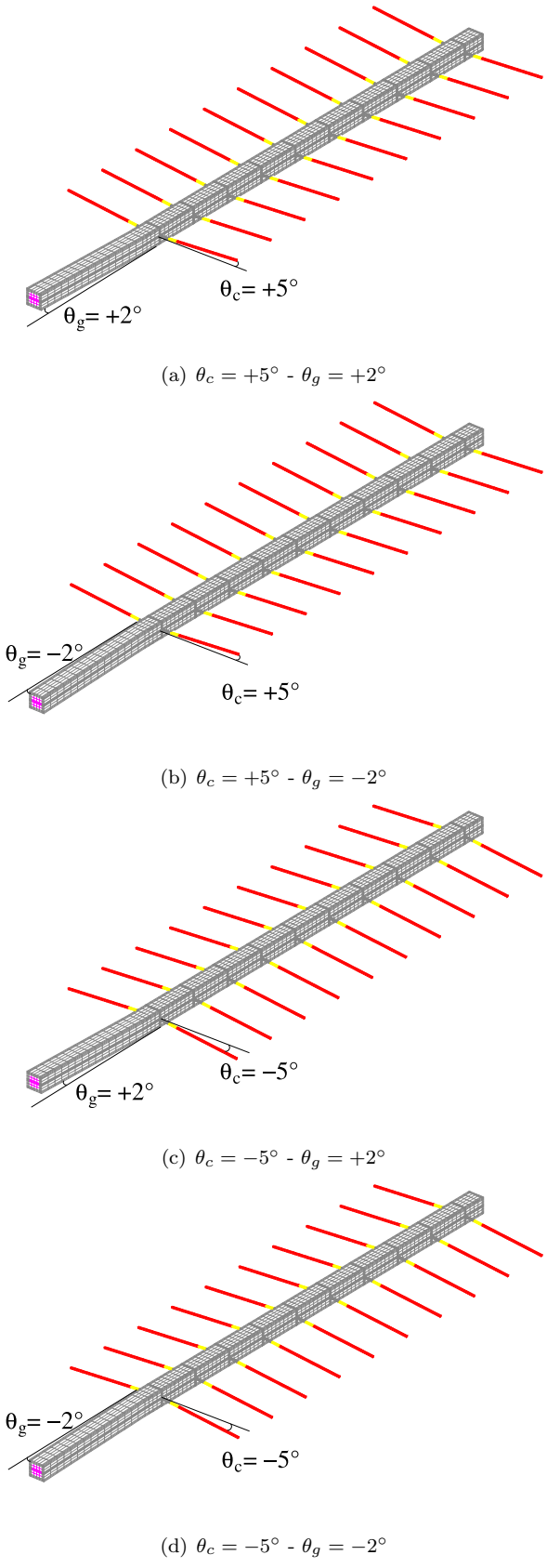

(a) $\theta_c = +5°$ - $\theta_g = +2°$

(b) $\theta_c = +5°$ - $\theta_g = -2°$

(c) $\theta_c = -5°$ - $\theta_g = +2°$

(d) $\theta_c = -5°$ - $\theta_g = -2°$

Fig. 5 Repository unit altered geometries.

4.2 Mesh description

The meshes used for the numerical simulation were built using the mesh generation tool in CASTEM [13]. The object oriented programming language of CASTEM allows the user to define the angles θ_g and θ_c as parameters. For all parameter values, we constructed meshes with an identical number of 361,800 cells (380,835 nodes). An example of the mesh built with parameter values $\theta_g = -2°$ and $\theta_c = +5°$ is presented in Figure 6.

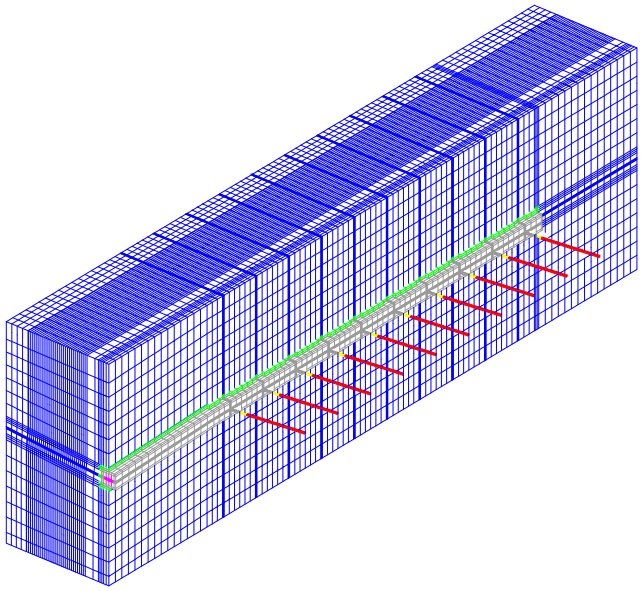

Fig. 6 Mesh built for angle deviations set $\theta_g = -2°$ and $\theta_c = +5°$.

4.3 Material Properties (hydraulics)

Permeability values needed by (1) for the different materials constituting the repository unit, including drift backfill, concrete, bentonite, vitrified waste, EDZ and argillaceous host rock are given in Table 2. The argillaceous host rock is considered anisotropic.

Table 2 Permeability values of the engineered barrier materials, waste and host rock

Material	Permeability ($m.s^{-1}$)
Argillaceous host rock	10^{-13} (v) / 10^{-12} (h) [17,18,25]
EDZ	5×10^{-11} [2,17]
Vitrified waste	10^{-8} [22]
Concrete	10^{-10} [22]
Bentonite	10^{-11} [2,6]
Gallery backfill	10^{-6} [2,22]

4.4 Material Properties (transport)

We chose to perform an iodine (^{129}I) transport calculation which is the most relevant radionuclide for performance assessment calculations due to the large amount of iodine included in vitrified waste, its high mobility and its very low decay constant. Intrinsic transport properties of iodine are given in Table 3. The useful material properties to consider for transport computations are the porosity ω, the effective diffusion coefficient D_e and the longitudinal and transverse dispersivities α_L and α_T (Cf. Eq. 2). The effective diffusion coefficient is expressed as $D_e = \omega\tau D_0$ [30] with D_0 the molecular diffusion coefficient (given in Table 3 for iodine) and τ [−] the tortuosity. Useful values are synthetised in Table 4. Note that at the initial radionuclide release time, waste steel canisters are assumed to be fully corroded and vitrified waste is treated as a highly fractured media with a given permeability and porosity.

Table 3 Intrinsic transport properties of iodine (^{129}I).

Molecular diffusion coefficient D_0 $(m^2 \cdot s^{-1})$	λ (s^{-1})
1.08×10^{-9}	1.4×10^{-15}

Table 4 Transport parameters for each repository material

Material	ω	τ	D_e	α_L - α_T
Argillaceous host rock	0.06	0.1	6.5×10^{-12}	1 - 0.1
EDZ	0.20	0.1	2.2×10^{-11}	1 - 0.1
Vitrified waste	0.10	0.1	1.1×10^{-11}	1 - 0.1
Concrete	0.20	0.1	2.2×10^{-11}	1 - 0.1
Bentonite	0.20	0.1	2.2×10^{-11}	1 - 0.1
Gallery backfill	0.40	0.3	1.3×10^{-10}	1 - 0.1

4.5 Initial and boundary conditions

4.5.1 Hydraulics

The flow direction in the repository unit is assumed to be essentially in the positive vertical direction and arise from a vertical head gradient of 1 [22,36]. We chose to impose east and west vertical boundaries of the domain to be no-flow boundaries. The top and bottom head boundaries are fixed to $350\,m$ and $450\,m$ respectively. The north and south head boundaries conditions are linear in z. The values of the imposed boundary conditions (Dirichlet or Neumann) on the different boundaries of the computational domain are summarized in Table 5.

Table 5 Imposed hydraulic boundaries. Coordinate y varies from 0 (South surface) to $Lyt \simeq 323\,m$ (North surface) and coordinate z from 0 (bottom surface) to $Hhr = 100\,m$ (top surface).

Boundaries	Head (m)
Top surface	350
Bottom surface	450
East and West surface	No flow
South surface	$450 - z$
North surface	$450 - z$

4.5.2 Transport

At the initial computation time, the iodine concentration is set to zero throughout the system.

The boundary conditions for the transport calculations have been chosen in order to match the symmetries of the repository or the physical phenomena in the test case system (activity dilution in the surrounding aquifers, activity diffusion throughout the system). Boundary conditions were chosen to ensure a no flux condition on east and west boundary for symmetry reasons. As no convective flux occurs on those boundaries due to no flow boundary conditions (see hydraulic boundary conditions), the no flux condition is equivalent to a no-diffusive flux condition. A zero concentration was imposed on the bottom boundary in order to ensure that incoming water in the system is free of pollutants (incoming fresh water). A zero concentration was imposed on the top boundary where fast upper aquifer flow is assumed to dilute the pollutant (dilution in fresh water). We chose to impose a zero concentration on north and south boundaries in order to ensure that incoming water in the system is free of pollutants. Note that a zero concentration imposition implies that the outflux is then only diffusive on those surfaces.

The source term Q $[mol \cdot m^{-3} \cdot s^{-1}]$, located inside the vitrified waste, is assumed to be a constant release for the first 1,000 years after canister failure. The time needed for the full radionuclide release is then $t_s = 1,000$ years. We arbitrarily set $Q = 1/V_s t_s\, mol \cdot m^{-3} \cdot s^{-1}$, where V_s is the volume of the waste canisters ($V_s = 230.64\,m^3$), leading to a total arbitrary amount of released iodine inside the system of $M = QV_s t_s = 1\,mol$.

4.6 Numerical indicators

In order to compare our numerical results for different parameters values we use the stationary head distribution field as well as the velocity field in the repository system. The iodine plume field inside the system at different times is also of interest. But those data are difficult to use for performance comparison purposes. We then define and compute an output flux from the domain as a function of time. This output flux is defined as the total flux (convective and diffusive) that escapes the system across a top horizontal surface located about 36 meters above the source and across a vertical plane located 48 meters from the south system border. We are then able to evaluate the total flux escaping the system, including the mainly diffusive flux across the host rock and the mainly convective flux across the connecting gallery. We consider the peak value of this flux to be a numerical repository performance criteria that allows quantitative comparison. The lower the peak value, the better the repository performance.

5 Numerical results

5.1 Reference repository geometry

5.1.1 Hydraulics

The head distribution field calculated for the reference repository geometry is presented in Figure 7. The head

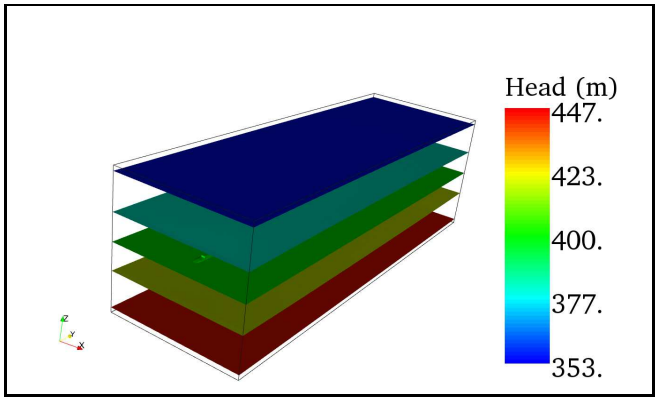

Fig. 7 Head isovalues calculated for the reference repository geometry.

isovalues shown in Fig. 7 correspond to $H = 355$, 380, 400, 420 and 445 meters and indicate that the water flow inside the system is mainly directed upward. From Figure 7, it is not possible to see any significant influence of the repository on the head field.

Nevertheless the calculated flow field presented in Figure 8 allows us to describe the impact of the repository on the flow field inside the system. Note that this flow field is presented using a logarithmic scale for the norm of the velocity. Figure 8 presents an essentially upward flow field in the host rock as expected from the head isovalues shown in Fig. 7. The flow velocity in the

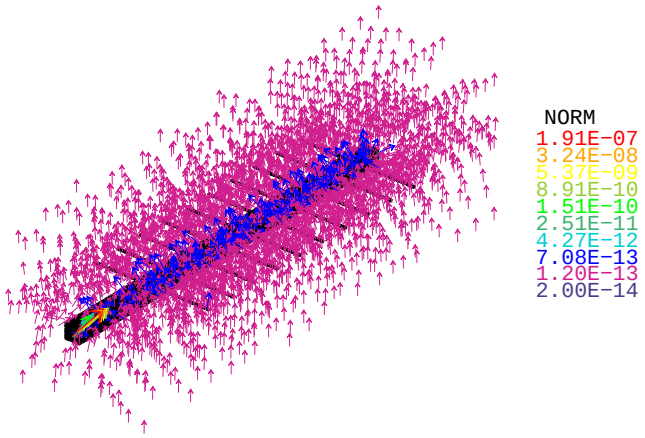

Fig. 8 Flow field (log scale) calculated for the reference repository geometry.

host rock is small with a value of about $10^{-13}\,m\cdot s^{-1}$ which is in agreement with the order of velocity magnitude expected in the host rock from a vertical permeability of $10^{-13}\,m\cdot s^{-1}$ and a vertical head gradient of $1\,m/m$. The vertical flow field is slightly perturbed at the vicinity of the repository where the repository collects the water coming from the bottom of the host rock and releases it vertically toward the host rock top. The largest values of the velocity field are located at the gallery entrance (south border of the system) where water enters the bottom part and escapes the upper part of the gallery entrance. Note that the shape of the flow field at the gallery entrance is due to the intersection of the imposed linear vertical head on the south border with the high permeability contrast between the gallery and the anisotropic host rock. Note that the flow field in this part of the system must be considered as a numerical modelling artifact and must not be taken into account for repository performance analysis.

For a better understanding of the flow path inside the repository system, Figure 9 focuses on the underground repository velocity field. Figure 9 shows that the upward flow field inside the bottom part of the host rock is collected by the connecting gallery and by the repository cells and immediately released towards the top of the host rock. The vertical velocity inside the repository cells is about $2.5\times10^{-13}\,m\cdot s^{-1}$ (twice the host rock velocity) and about $10^{-12}\,m\cdot s^{-1}$ in the gallery backfield (one order of magnitude higher than in the host rock). Figure 9 does not show any preferential flow inside the repository structure except at the connecting gallery entrance.

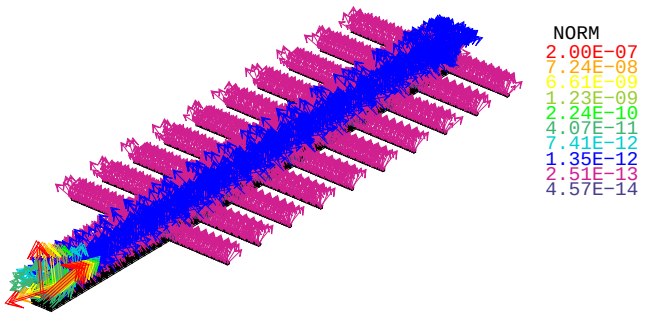

Fig. 9 Flow field (log scale) inside the works calculated for the reference repository geometry.

5.1.2 Transport

Figure 10 shows the transport computation results obtained for the reference geometry in terms of radionuclide plume inside the system at time $t = 10,000, 25,000, 50,000, 100,000, 250,000$ and $500,000$ years.

The radionuclide transport pathway inside the repository system is extracted from Figure 10 and Figures 8 and 9. The radionuclides initially contained inside the vitrified waste (see Figure 6) are released upward in the host rock (see Figures 8 and 9) where individual repository cell plumes spread because of diffusive and dispersive processes. Figure 10 indicates that the transport process is mainly diffusive and that the convection process inside the host rock is low (cell mesh Péclet $Pe = 0.07$). Indeed, the spreading individual plumes centered on repository cells (see Figure 10(a)) merge to two larger plumes centered on the repository cell row (see Figure 10(b), 10(c) and 10(d)) before merging into a unique plume centered on repository system (see Figure 10(e) and 10(f)).

The radionuclide output flux defined in section 4.6 and calculated for the reference geometry is presented as a function of time in Figure 11. Figure 11 shows an

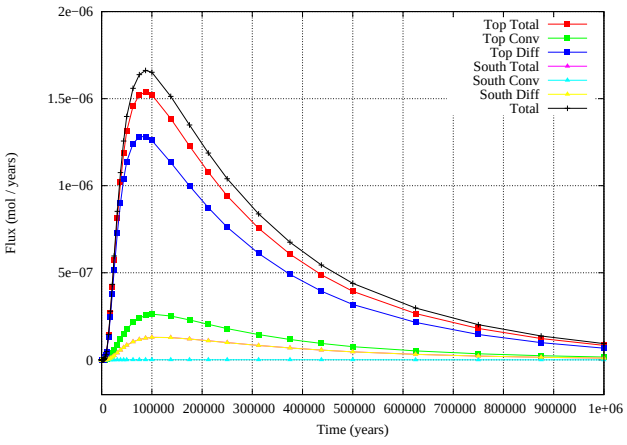

Fig. 11 Radionuclide output flux evolution.

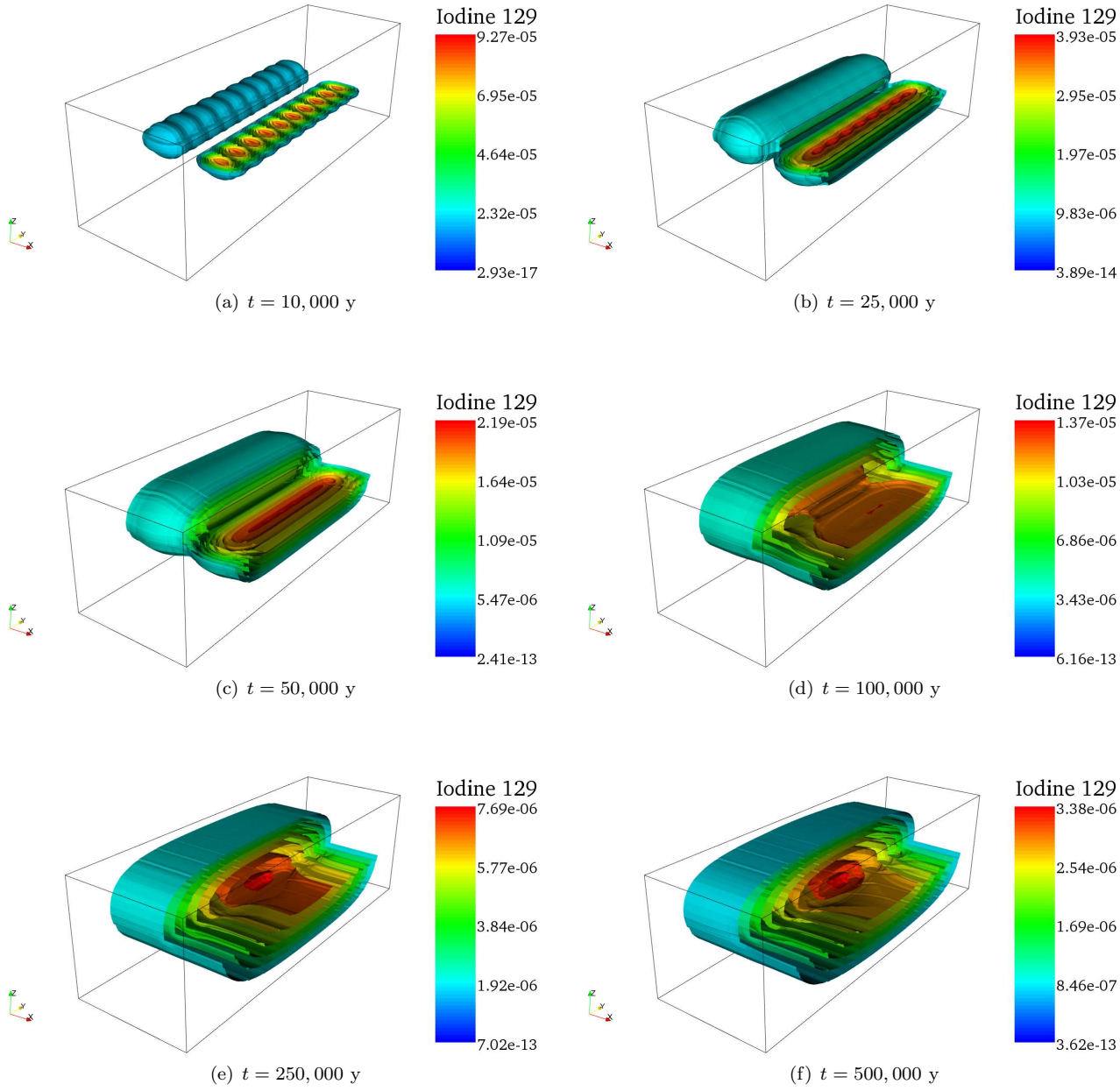

(a) $t = 10,000$ y (b) $t = 25,000$ y

(c) $t = 50,000$ y (d) $t = 100,000$ y

(e) $t = 250,000$ y (f) $t = 500,000$ y

Fig. 10 Concentration isosurfaces ($mol \cdot m^{-3}$) of iodine plume in the repository at different times. Cut view where the upper right part of the system is removed.

arrival time of the iodine peak at $t = 87,500\,y$ for a peak value of $1.66 \times 10^{-6}\,mol \cdot y^{-1}$. Note that the peak value of the flux calculated here has no radiological signification and will only be used for performance comparison purposes.

Figure 11 indicates that the major contribution to the total output flux arises from the top inner control surface. On this surface, the diffusive flux is, as observed in Figure 10, the dominant process with a convective flux five times lower. Note that the order of magnitude of the diffusive arrival time at the top inner control surface can be expressed as $T_D = L^2/4D_p$ where $L = 36\,m$ is the distance between the source and the control surface and where $D_p = D_e/\omega$ ($\simeq 1.1 \times 10^{-10} m \cdot s^{-2}$ for the argillaceous host rock) is the pore diffusion coefficient. We then obtain $T_D \simeq 93,000\,y$ which is in agreement with the results in Figure 11. Note that the order of magnitude of the convective arrival time at the top

inner control surface can be expressed as $T_C = L/V_p$ where $V_p = U/\omega$ ($\simeq 8 \times 10^{-12} m \cdot s^{-1}$ for the argillaceous host rock) is the pore velocity. We obtain $T_C \simeq 137,000\, y$ which agrees with the results in Figure 11.

On the vertical inner south control surface, the convective flux is zero as expected from the vertical calculated flow field and the total flux reduces to a small diffusive flux ten times lower than the diffusive flux on the top inner control surface.

5.2 Altered repository geometries

5.2.1 Hydraulics

The head isovalues and the flow field calculated for each of the four altered repository geometries are very similar to the ones depicted in Figures 7 and 8. For each case, those data only indicated that the flow field is directed mainly vertical upward (data not shown). We then focus on the velocity field inside the repository in order to obtain a more precise picture of the flow inside the repository system. The flow fields corresponding to the geometries depicted in Figure 5 are presented in Figure 12.

Figure 12 shows that for the altered geometries where $\theta_c = -5°$ the vertical water flow inside the host rock collects from the dead ends of the repository cells towards the connecting gallery. The flow is then mainly directed towards the top of the host rock with a small amount of water directed from the connecting gallery towards the connecting gallery entrance when $\theta_g = +2°$ and from the connecting gallery entrance towards the connecting gallery for $\theta_g = -2°$.

For the altered geometries where $\theta_c = +5°$, the vertical water flow inside the host rock is collected from the connecting gallery towards the dead ends of the repository cells and then upward to the host rock top. The influence of θ_g is the same than previously depicted.

In all the cases, the velocity value inside the first part of the connecting gallery backfill (part from the southern entrance to the middle of the cell repository system) is of about $10^{-11}\, m \cdot s^{-1}$ and is of about $2 \times 10^{-12}\, m \cdot s^{-1}$ in the second part (part from the middle of the cell repository system to the dead end connecting gallery).

For the geometries where θ_c and θ_g are of the same sign (the center of the connecting gallery is then at the top or at the bottom of the whole repository system) the velocity value inside the repository cells is of about $10^{-11}\, m \cdot s^{-1}$. But, for the cases where θ_c and θ_g are of the opposite sign (the elevation between the connecting gallery entrance and the repository cells dead ends is maximum) the velocity inside the repository cells reaches a maximum value of about $6 \times 10^{-11}\, m \cdot s^{-1}$.

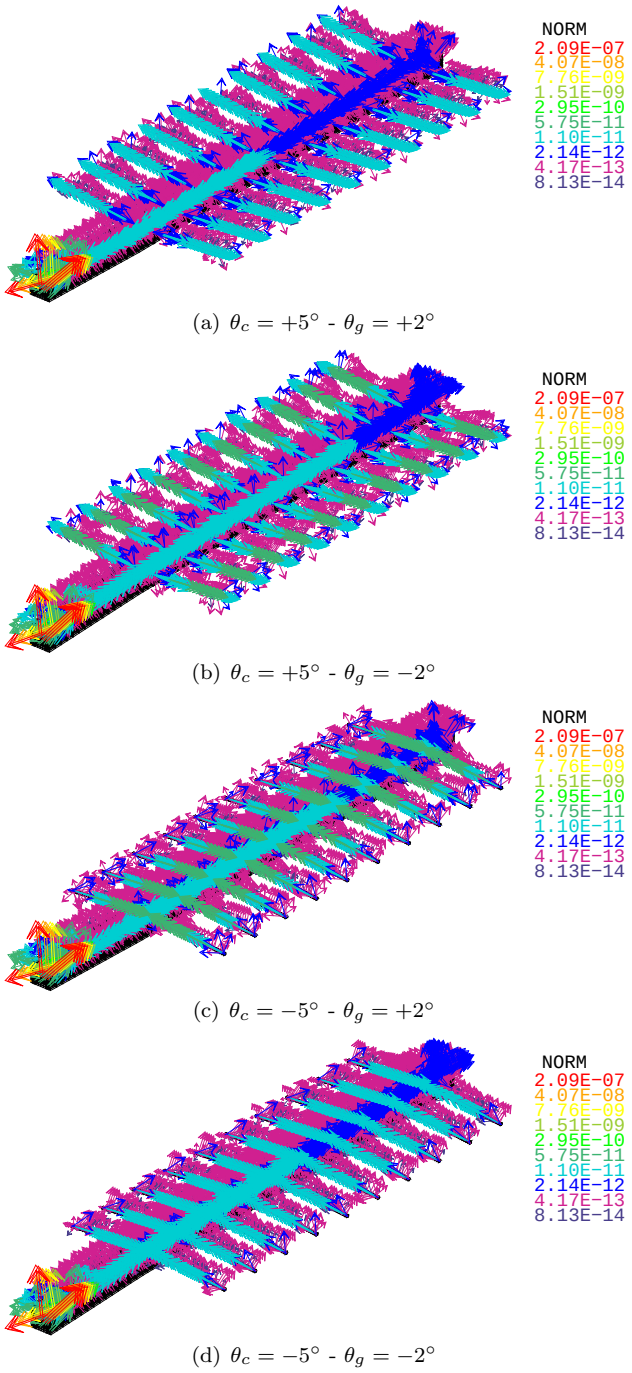

(a) $\theta_c = +5°$ - $\theta_g = +2°$

(b) $\theta_c = +5°$ - $\theta_g = -2°$

(c) $\theta_c = -5°$ - $\theta_g = +2°$

(d) $\theta_c = -5°$ - $\theta_g = -2°$

Fig. 12 Flow fields calculated for the altered geometries.

The calculated flow fields presented in Figure 12 clearly show that the repository cells and gallery deviations from the horizontal strongly modify the flow inside the repository. The deviations create a preferential flow in the system with direction in the repository cells and in the gallery entrance depending on the signs

of θ_c and θ_g. The flow velocity in the repository is also strongly affected with an increase of about one order of magnitude.

5.2.2 Transport

We performed transport computations for the four altered geometries depicted in Figure 5.

Figure 13 shows the transport computation results obtained for the altered geometry where $\theta_c = +5°$ and $\theta_g = +2°$ in terms of radionuclide plume inside the system at time $t = 10,000$, $25,000$, $50,000$, $100,000$, $250,000$ and $500,000$ years. Figure 14 shows the transport computation results obtained for the altered geometry where $\theta_c = -5°$ and $\theta_g = -2°$ in terms of radionuclide plume inside the system at time $t = 10,000$, $25,000$, $50,000$, $100,000$, $250,000$ and $500,000$ years. The results obtained for the altered geometry where $\theta_c = +5°$ and $\theta_g = -2°$ and for the altered geometry where $\theta_c = -5°$ and $\theta_g = +2°$ are very similar to the ones presented in Figure 13 and Figure 14 respectively and are not presented.

The radionuclide transport pathway inside the repository systems is obtained from Figures 13 and 14. In all cases, the radionuclides initially contained inside the vitrified waste (see Figure 6) are released upward in the host rock where the individual repository cell plumes spread because of diffusive and dispersive processes. Figures 13 and 14 indicate, as for the reference case, that the transport process is mainly diffusive and that the convection process inside the host rock is low. Indeed, spreading individual plumes centered on repository cells (see Figures 13(a) and 14(a)) merge to two larger plumes centered on the repository cell row (see Figures 13(b) and 14(b), 13(c) and 14(c), 13(d) and 14(d)) before merging into a unique plume centered on the repository system (see Figures 13(e) and 14(e), 13(f) and 14(f)). The impact of the flow direction inside the cell repository is small and only observable when comparing Figures 13(d) and 14(d). The influence of the inclination of the gallery entrance is more visible and varies from a no radionuclide flow for the reference case (see the flat iso-concentration shape at the front of Figure 10(e)) to an output flow in the $\theta_c = +5°$ and $\theta_g = +2°$ case (see the hump iso-concentration shape at the front of Figure 13(e)) and to an input flow in the $\theta_c = -5°$ and $\theta_g = -2°$ case (see the trough iso-concentration shape at the front of Figure 14(e)).

The radionuclide output flux defined in section 4.6 was computed for each altered geometry and presented in Figures 15 to 18.

As for the reference case, Figures 15, 16, 17 and 18 indicate that the major contribution to the total

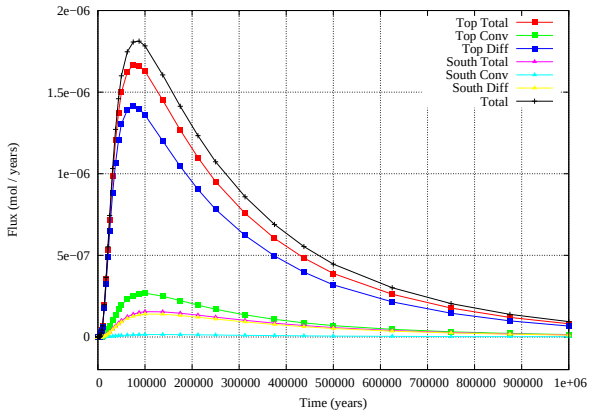

Fig. 15 Radionuclide output flux evolution for $\theta_c = +5°$ and $\theta_g = +2°$ geometry.

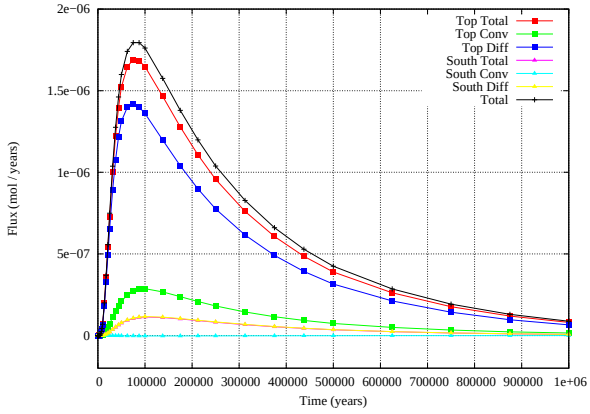

Fig. 16 Radionuclide output flux evolution for $\theta_c = +5°$ and $\theta_g = -2°$ geometry.

output flux stems from the top inner control surface. On this surface, diffusive flux is, as shown in Figs. 13-14, the dominant process with a convective flux five times lower.

Figures 15-16 show an arrival time of the iodine peak at about $t = 87,500\,y$ whereas Figs. 17-18 show a delayed arrival time at about $t = 100,500\,y$. The arrival time delay induces a decrease of the iodine peak value because of longer diffusive process action.

The comparison of the Figures 15 to 18 allows us to extract the particular effects of θ_c and θ_g on the results. As seen in Figures 15, 16, 17 and 18, the larger impact on the results is due to θ_c which mainly acts on the top inner control surface flux. The change of $\theta_c = +5°$ into $\theta_c = -5°$ delays the diffusive and convective arrival time on the top inner control surface of about $20,000\,y$ and induces a decrease of the iodine peaks. Note that this delay corresponds to the change in distance of the radioactive waste barycenter system to the top inner control surface. The θ_g impact is smaller and mainly

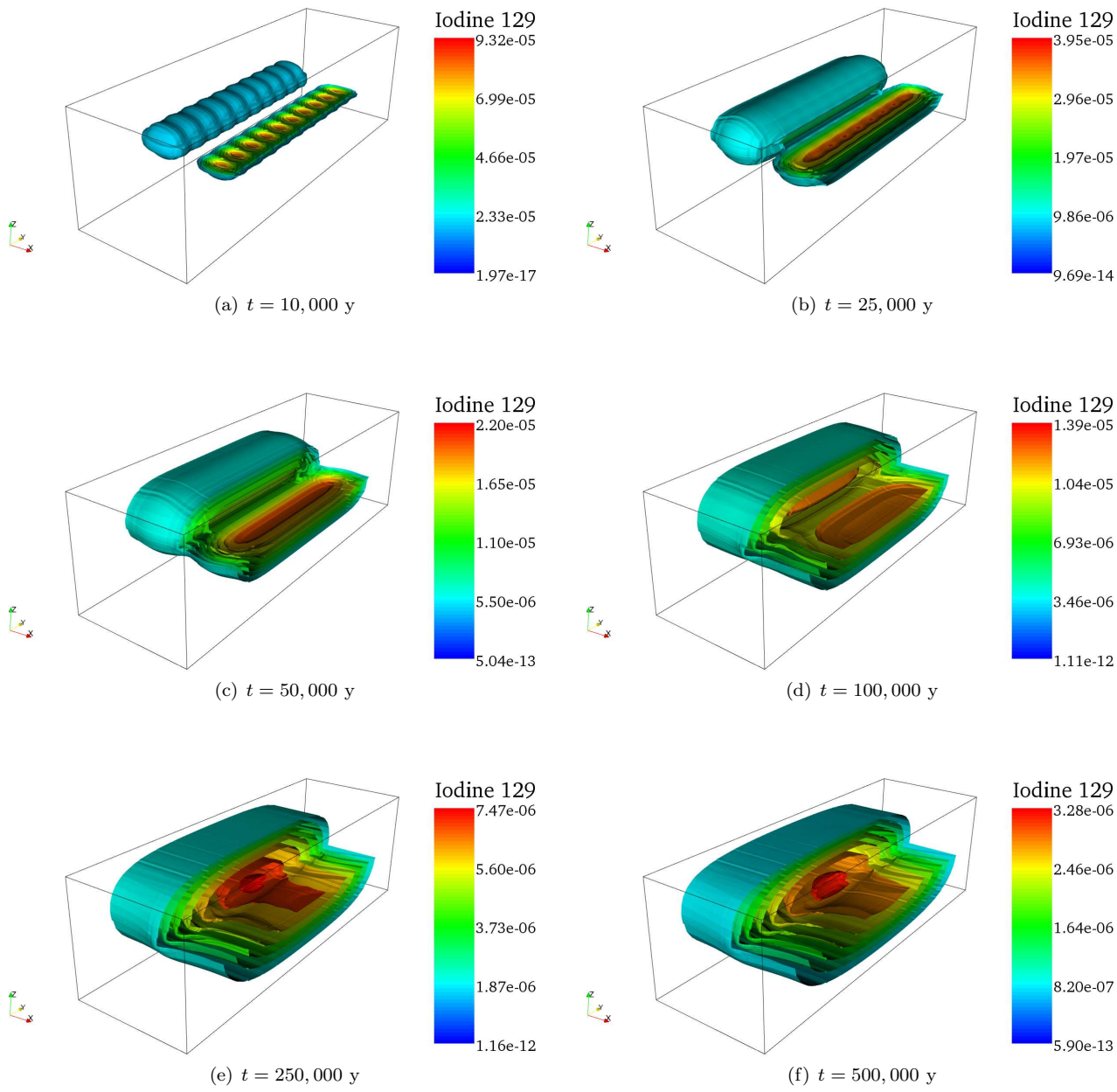

Fig. 13 Concentration isosurfaces ($mol \cdot m^{-3}$) of iodine plume in the repository ($\theta_c = +5°$ and $\theta_g = +2°$) at different times. Cut view where the upper right part of the system is removed.

acts on the convective flow on the south vertical control surface (compare Figures 15 and 17 to Figures 16 and 18 respectively). When $\theta_g = +2°$ a convective outflow occurs inside the gallery whereas when $\theta_g = -2°$ the flow inside the gallery towards the repository induces a very small negative convective flux.

In order to compare the effects of θ_c and θ_g on the repository performance, the radionuclide total output fluxes for each altered geometry are compared to the one computed for the reference geometry in Figure 19. Figure 19 shows that, in terms of performance isolation, the best repository geometry is the $\theta_c = -5°$ and $\theta_g = -2°$ geometry with an iodine peak value of $1.55 \times 10^{-6}\, mol \cdot y^{-1}$ and the worst is the $\theta_c = +5°$ and $\theta_g = +2°$ geometry with an iodine peak value of $1.81 \times 10^{-6}\, mol \cdot y^{-1}$. The best geometry does not present an outflow inside the connecting gallery (with $\theta_g = -2°$) and maximize the diffusive and convective vertical path

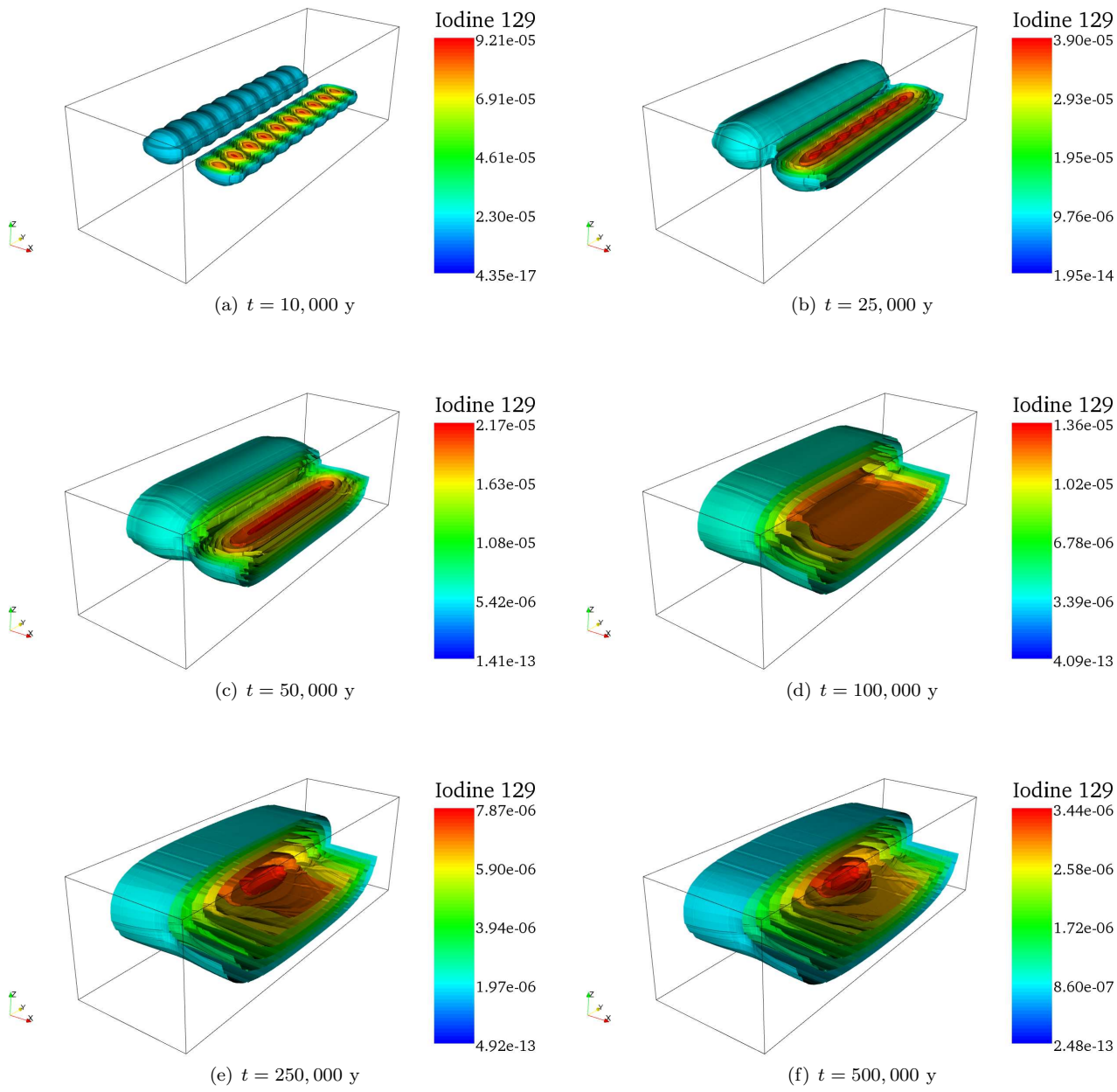

(a) $t = 10,000$ y (b) $t = 25,000$ y

(c) $t = 50,000$ y (d) $t = 100,000$ y

(e) $t = 250,000$ y (f) $t = 500,000$ y

Fig. 14 Concentration isosurfaces ($mol \cdot m^{-3}$) of iodine plume in the repository ($\theta_c = -5°$ and $\theta_g = -2°$) at different times. Cut view where the upper right part of the system is removed.

by lowering the radionuclide source barycenter (with $\theta_c = -5°$).

The worse-case geometry increases of 9 percent of the peak value in comparison to the reference geometry and the best-case geometry decreases of 7 percent of the peak value.

6 Conclusion

We conducted flow and radionuclide transport calculations on radioactive waste repository geometries taking into account potential repository cells and gallery deviation from the horizontal. The results obtained showed that, even for few degrees of deviation, the radionuclides transport pathway in the repository system is modified and can result in an increase of the maximum radionu-

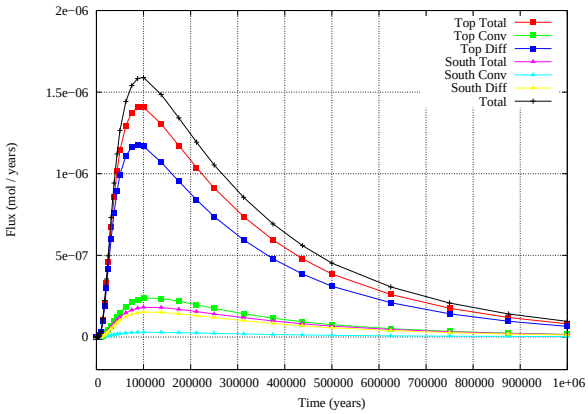

Fig. 17 Radionuclide output flux evolution for $\theta_c = -5°$ and $\theta_g = +2°$ geometry.

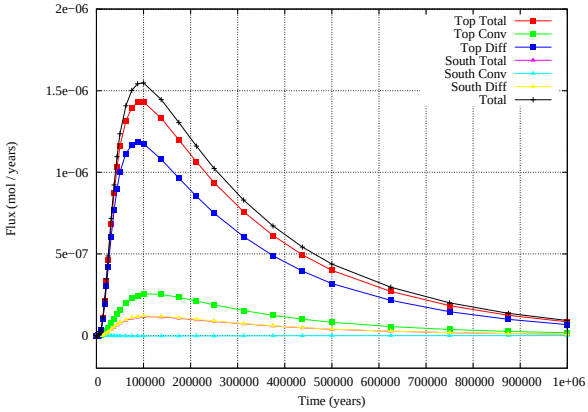

Fig. 18 Radionuclide output flux evolution for $\theta_c = -5°$ and $\theta_g = -2°$ geometry.

clide activity release from the repository of about 9 percent.

Those results lead to two major conclusions. First, if the potential deviation of the repository cells and connecting gallery during the repository construction can not be fully controlled, the worse-case geometry configuration must be considered for performance assessment. In the case of a vertical upward dominant flow field, this worse-case geometry corresponds to the case were the repository cells and the connecting gallery are drilled with the same upward deviation. If not, the use of a classic perfect horizontal geometry will result in the underestimation of the maximum radionuclide activity release peak of about 9 percent.

Second, in the case of a vertical upward flow configuration, the geometry including a downward deviation of the repository cells and a downward deviation of the connecting gallery is of interest. Thus, this slight modification of the geometry in comparison to the classical horizontal one could result in a decrease of the radionuclides flux peak value of about 7 percent (and a 16 percent decrease from the worse-case geometry case).

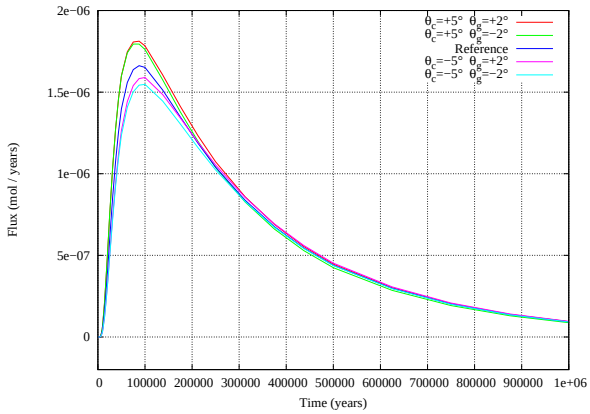

Fig. 19 Radionuclide total output flux evolutions for all considered geometries.

Acknowledgements The work presented in this paper was partly founded through the Euratom project PAMINA (Performance Assessment Methodologies in Application to Guide the Development of the Safety Case - FP6-036404).

The authors acknowledge Donna Calhoun for proof reading of the article and providing many useful suggestions.

References

1. Aavatsmark I, Barkve T, Boe O, Mannseth T. Discretization on unstructured grids for inhomogeneous, anisotropic media, Part I: Derivation of the methods. Siam J Sci Comput 1998;195:1700-1716.
2. Dossier 2005 Argile. Évaluation de la faisabilité du stockage géologique en formation argileuse. ANDRA report, ISBN 2-951 0108-8-5, juin 2005, 240 p.
3. Barrett R, Berry M, Chan T F, Demmel J, Donato J, Dongarra J, Eijkhout V, Pozo R, Romine C, Van der Vorst H. Templates for the Solution of Linear Systems : Building Blocks for Iterative Methods. Philadelphia, USA. SIAM, 1994.
4. Bäckblom G, Christiansson R, Lagerstedt L. Choice of rock excavation methods for the Swedish deep repository for spent nuclear fuel. SKB report R-04-62, ISSN 1402-3091, September 2004, 146 p.
5. Bernard-Michel G, Le Potier C, Beccantini A, Gounand S, Chraibi M. The Andra Couplex1 test: Comparison between Finite Element, Mixed Hybrid Finite Element and Finite Volume Element discretizations: Simulation of transport around a nuclear waste disposal Site. Comput Geosci 2004;8:187-201.
6. Blümling P. Borehole sealing project at the Grimsel Test Site. Geotechnical and Geological Engineering 2005;23:843-858.
7. Blümling P, Bernier F, Lebon P, Martin C D. The excavation damaged zone in clay formations time-dependent behaviour and influence on performance assessment. Physics and Chemistry of the Earth 2007;32:588-599.
8. Bollingerfehr W, Filbert W, Bosgiraud J-M, Haverkate B. ESDRED Module 2 Final Report: Waste canister transfer and emplacement technology. European Commission Report (Contract Number: FI6W-CT-2004-508851), 2009, 78 p.

9. Bossart P, Meier P M, Moeri A, Trick T, Mayor J-C. Geological and hydraulic characterisation of the excavation disturbed zone in the Opalinus Clay of the Mont Terri Rock Laboratory. Engineering Geology 2002;66:19-38.
10. Bourgeat A, Kern M, Schumacher S, Talandier J. The COUPLEX test case: Nuclear waste disposal simulation. Computational Geosciences 2004;8:83-98.
11. Brezzi F, Fortin M. Mixed and Hybrid Finite Methods. New York, USA: Springer-Verlag, 1991.
12. Cai M, Kaiser P K. Assessment of excavation damaged zone using a micromechanics model. Tunnelling and Underground Space Technology 2005;20:301-310.
13. CEA. CASTEM 2000 User's Manual, english Version. http://www-cast3m.cea.fr.
14. Claesson L-Å, Nilsson G, Ullberg A. Forsmark site investigation. Drilling of the traditional cored borehole KFM07B and the telescopic borehole KFM07C at drill site DS7. SKB report P-06-170, ISSN 1651-4416, April 2007, 54 p.
15. Cormenzana J L, Grupa J, Cuñado M A, Becker D A, Bolado R, Pepin G, Plas F, Hart J, Fischer-Appelt K, Badea A, Schröder T J, Röhlig K-J, Ávila R, Rosca-Bocancea E, Plischke E, Spießl S. Lessons learnt from studies on sensitivity analysis techniques in the EU project PAMINA: Sensitivity analysis applied to different HLW PA models. Reliability, Risk, and Safety. Theory and Applications. Edited by Guedes Soares C, Briš R and Martorell S, ISBN 978-0-415-55509-8, CRC Press 2010.
16. Dabbene F. Mixed Hybrid Finite Elements for Transport of Pollutants by Undergrounds Water. Proc. of the 10^{th} Int. Conf. on Finite Elements in Fluids, Tucson USA, 1998.
17. Davy, C.A., Skoczylas, F., Barnichon, J.-D., Lebon, P.: Permeability of macro-cracked argillite under confinement: Gas and water testing. Physics and Chemistry of the Earth, 2007;32:667-680
18. Delay J, Trouiller A, Lavanchy J-M. Propriétés hydrodynamiques du Callovo-Oxfordien dans l'Est du bassin de Paris : comparaison des résultats obtenus selon différentes approches. C R Geoscience 2006;338:892907.
19. Ebashi T, Hwang Y-S, Lee Y-M, Ohi T, Koo S. Application of the comprehensive sensibility analysis method to a Korean geological disposal concept. J of Nuclear Science and Technology 2008;45(11):1138-1149.
20. Eisner L, Petr B, Le Calvez J H. Borehole deviation surveys are necessary for hydraulic fracture monitoring. Society of Exploration Geophysicists Annual Conference and Exhibition, New Orleans, October 2006; 359-362.
21. URANIE: The CEA/DEN uncertainty and sensivity platform. Procedia social and behavioral sciences 2010;2:7660-7661.
22. Genty A, Mathieu G, Weetjens E. Final report on benchmark calculation in clay. PAMINA (Performance Assessment Methodologies in Application to Guide the Development of the Safety Case) Deliverable (D-N:4.2.4). European Commission under the Euratom Research and Training Programme on Nuclear Energy within the Sixth Framework Programme (2002-2006) Report (Contract Number: FP6-036404), 2009.
23. GoldSim Technology Group LLC. Goldsim Contaminant Transport User's Guide, http://www.goldsim.com 2011.
24. Helton J C. Uncertainty and sensivity analysis in performance assessment for the Waste Isolation Pilot Plan. Computer Physics Communications 1999;117:156-180.
25. Homand F, Shao J-F, Giraud A, Auvray C, Hoxha D. Pétrofabrique et propriétés mécaniques des argilites. C R Geoscience 2006;338:882891.
26. Hudson J A, Bäckström A, Rutqvist J, Jing L, Backers T, Chijimatsu M, Christiansson R, Feng X-T, Kobayashi A, Koyama T, Lee H-S, Neretnieks I, Pan P-Z, Rinne M, Shen B-T. Characterising and modelling the excavation damaged zone in crystaline rock in the context of radioactive waste disposal. Environ Geol 2009;57:1275-1297.
27. Le Potier C. Finite volume in 2 or 3 dimensions for a diffusion convection equation applied to porous media with Cast3m. Proc of the XVIth Int Conf on Computational Methods in Water Resources, Chapel Hill USA 2004, Elsevier, p 1015-1026.
28. Levasseur S, Charlier R, Frieg B, Collin F. Hydro-mechanical modelling of the excavation damaged zone around an underground excavation at Mont Terri Rock Laboratory. Inter J of Rock Mechanics & Mining Sciences 2010;47:414-425.
29. Marpeau F, Saad M. 3D simulation of radionuclide transport in porous media. Int. J. Numer. Meth. Fluids 2010;64:44-70.
30. de Marsily G. Quantitative Hydrogeology. San Diego, USA: Academic Press, 1986.
31. Millard A, Maßmann J, Rejeb A, Uehara S. Study of the initiation and propagation of excavation damaged zones around openings in argillaceous rock. Environ Geol 2009;57:1325-1335.
32. Mügler C, Genty A, Cabrera J. Numerical modelling of hydraulic decompression due to the excavation of tunnel and drifts at the Tournemire underground laboratory. Geotechnical and Geological Engineering 2004;22:525-543.
33. Murphey C E, Cheatham J B. Hole deviation and drill string behavior. SPE Journal 1966;6(1):44-54.
34. Neuzil CE. How permeable are clays and shales? Water Resources Research 1994;30(2):145-150.
35. Perraud D, Pepin G, Treille E, Loth L, Bolado-Lavín R, Nilsson K-F, Prváková S, Costescu-Badea A. Final report on uncertainty analysis codes (D 4.3.1), EU project PAMINA: Performance Assessment Methodologies in Application to Guide the Development of the Safety Case (Contract Number: FP6-036404), http://www.ip-pamina.eu/publications/reports/index.html 2009.
36. Prváková S, Bolado-Lavín R, Badea A, Nilsson K-F, Pepin G, Treille E. First benchmark for the uncertainty analysis based on the example of the French clay site results. European Commission Joint Research Centre Institute for Energy. JRC 41828, EUR 23228 EN, ISSN 1018-5593, European Communities, 137 p, 2008.
37. Rothfuchs T, Brewitz W. Radioactive waste disposal in geological salt formation - current concepts, possible improvements and status of field testing. Proc of the 6^{th} Int Conf on Field Measurements in Geomechanics, Olso 2003, Myrvoll (ed.), Swets & Zetlinger, Lisse, The Nertherlands, ISBN 90 5809 602 5, p 307-312.
38. Sedlák V. Magnetic induction applied to borehole deviation problems. Geotechnical and Geological Engineering 1993;11:25-35.
39. Stenberg L, Håkanson N. Oskarshamn site investigation. Revision of borehole deviation measurements in Oskarshamn. SKB report P-07-55, ISSN 1651-4416, September 2007, 409 p.
40. Thury M, Bossart P. The Mont Terri rock laboratory, a new international research project in a Mesozoic shale formation, in Switzerland. Engineering Geology 1999;52:347-359.
41. Van der Vorst H A. Bi-CGSTAB: A Fast and Smoothly Converging Variant of Bi-CG for the Solution of Nonsymmetric Linear Systems. SIAM Journal on Scientific and Statistical Computing 1992;13:631-644.
42. Verstricht J, Blümling P, Merceron T. Repository concepts for nuclear waste disposal in clay formations. Proc. of the 6^{th} Int Conf on Field Measurements in Geomechanics, Olso 2003, Myrvoll (ed.), Swets & Zetlinger, Lisse, The Nertherlands, ISBN 90 5809 602 5, p 387-392.
43. Voinov O V, Oganov G S, Reutov V A. Model of borehole deviation in anisotropic rock. Soviet Mining Science 1992;27(3):244-251.
44. Willenberg H, Evans K F, Eberhardt E, Loew S. Monitoring of complex rock slope instabilities - correction and analysis

of inclonometer/extensometer surveys and integration with surface displacement data. Proc. of the 6^{th} Int Conf on Field Measurements in Geomechanics, Olso 2003, Myrvoll (ed.), Swets & Zetlinger, Lisse, The Nertherlands, ISBN 90 5809 602 5, p 393-400.

45. Williamson H S. Accuracy prediction for directional measurement while drilling. Drilling and Completion 2000;15(4).
46. Wu F, Liu J, Liu T, Zhuang H, Yan C. A method for assessment of excavation damaged zone (EDZ) of a rock mass and its application to a dam foundation case. Engineering Geology 2009;104:254-262.
47. Yi M-J, Kim J-H, Son J-S. Borehole deviation effect in electrical resistivity tomography. Geosciences Journal 2009;13(1):87-102.